IEICE TRANS. COMMUN., VOL.E105–B, NO.6 JUNE 2022

INVITED PAPER *Special Section on Recent Progress in Antennas and Propagation in Conjunction with Main Topics of ISAP2020*

Analyses of Transient Energy Deposition in Biological Bodies Exposed to Electromagnetic Pulses Using Parameter Extraction Method

Jerdvisanop CHAKAROTHAI[†a)], **Katsumi FUJII**[†], **Yukihisa SUZUKI**[††], ***Members***, **Jun SHIBAYAMA**[†††], ***Senior Member***, ***and*** **Kanako WAKE**[†], ***Member***

SUMMARY In this study, we develop a numerical method for determining transient energy deposition in biological bodies exposed to electromagnetic (EM) pulses. We use a newly developed frequency-dependent finite-difference time-domain (FD^2TD) method, which is combined with the fast inverse Laplace transform (FILT) and Prony method. The FILT and Prony method are utilized to transform the Cole–Cole model of biological media into a sum of multiple Debye relaxation terms. Parameters of Debye terms are then extracted by comparison with the time-domain impulse responses. The extracted parameters are used in an FDTD formulation, which is derived using the auxiliary differential equation method, and transient energy deposition into a biological medium is calculated by the equivalent circuit method. The validity of our proposed method is demonstrated by comparing numerical results and those derived from an analytical method. Finally, transient energy deposition into human heads of TARO and HANAKO models is then calculated using the proposed method and, physical insights into pulse exposures of the human heads are provided.

key words: *specific energy absorption, Cole–Cole model, finite-difference time-domain, electromagnetic pulse*

1. Introduction

There are many applications of ultra-wideband (UWB) electromagnetic pulses (EMPs) including radars for military and commercial autonomous vehicles [1], non-destructive evaluation [2], [3], human vital signal detection [4], in-body/on-body communications [5], [6], and medical inspection and treatment [7], [8]. Despite the increasing use of EMPs, there are insufficient information and understanding of aspects of interactions between biological bodies and EMPs owing to the complexity in treating wide spectrum components of the EMPs and difficulties in treating the frequency dependence of the dielectric properties of biological media.

Nevertheless, the interactions between biological bodies and EMPs have been extensively investigated by numerical simulations and experiments. Recognized biological effects due to EMPs include the microwave hearing effect [9], [10], microwave heating effect [11], [12], and electroporation [13]. Microwave hearing is the phenomenon of perceiving an audible buzz or chirp sound as a result of energy absorption of microwave pulses by soft tissues inside the head [14], while the microwave heating effect is caused by the transformation of absorbed EM energy into heat. Note that the amount of absorbed energy may vary according to the location, tissue type, and geometrical factors of biological bodies, and hence it usually exhibits complex distribution depending on the exposed subject. Meanwhile, electroporation raises concern about the breakdown of lipid bilayer membranes at the cell level [15] and it may be excluded when considering macroscopic EM phenomena. To understand these phenomena correctly, distributions of the absorbed energy or induced EM fields inside biological bodies is essential.

Distributions of the absorbed energy and induced EM fields are governed by permittivity, conductivity, incident source configuration, and geometrical factors that describe the biological structure. In the literature, canonical shapes such as multilayer tissues, dielectric spheres, and prolate spheroidal models representing biological bodies were used as targets for the earliest investigation on interactions between EMPs and biological systems [16]–[18]. These studies derived the EM distribution at frequencies of interest, yet there is lack of information about the EM waveform inside the targets except in a few references, to the best of the authors' knowledge [19]. The main problem in deriving the pulse waveform inside biological bodies is due to the difficulty in incorporating the frequency dependence of the dielectric properties of the biological tissues, which is represented by the four-term Cole–Cole model [20]. Some studies adopted the fast Fourier transform or fast inverse Laplace transform (FILT) [21] in the calculation of the exact time-domain waveforms but a new calculation is required at every observation point inside biological bodies [22], [23]. As a result, large computational resources are needed in obtaining solutions across the whole analysis region.

To calculate the energy and EM distributions inside biological bodies, the finite-difference time-domain (FDTD) method has received much attention since it was proposed in 1966 [24]. This method uses a staggered grid model and adopts a leapfrog algorithm in advancing electric and magnetic field values at every point in the analysis space. Therefore, the induced current or specific absorption rate

Manuscript received July 6, 2021.
Manuscript revised October 13, 2021.
Manuscript publicized December 29, 2021.

[†]The authors are with National Institute of Information and Communications Technology, Koganei-shi, 184-8795 Japan.
[††]The author is with Tokyo Metropolitan University, Tokyo, 105-0011 Japan.
[†††]The author is with Hosei University, Koganei-shi, 184-8584 Japan.
a) E-mail: jerd@nict.go.jp

DOI: 10.1587/transcom.2021ISI0003

(SAR) inside a detailed human body can be found at once after the simulations ended. The popularity of the FDTD method is due to its capability to treat heterogeneous models in a straightforward manner and its high computation efficiency, as well as its high degree of affinity with large-scale parallelization using supercomputers [25], [26]. To evaluate exposure from a short pulse, many frequency-dependent finite-difference time-domain (FD^2TD) methods have been developed and used [27]–[30]. The methods use the first- or second-order Debye relaxation equation to express the complex permittivity of the medium. However, as shown in [31], even fourth-order Debye terms cannot provide sufficiently accurate and valid results for the transient EM distribution inside biological bodies. Recently, an alternative approaches using the Padé approximant or Riemann–Liouville theory to formulate the Cole–Cole relaxations have been proposed [32], [33]. The authors have also recently proposed a numerical approach combining the FILT and Prony method to formulate the Cole–Cole model. The proposed method has been successfully used to determine the specific energy absorption inside a numerical human head due to a single pulse [31], [34]. It has also been applied to design a UWB antenna for use in the vicinity of the human body [35].

In this paper, we develop a new FD^2TD approach, in which multiple Debye parameters extracted from the Cole–Cole model are incorporated with the aid of the FILT and the Prony method, for calculation of the transient energy deposition into biological bodies. Multiple Debye terms are formulated into the FDTD update equation by applying the auxiliary differential equation (ADE) method. The paper is outlined as follows. The proposed methodology of parameter extraction of the Cole–Cole relaxation model, the FDTD formulation of the update equation for the electric field, and the proposed algorithm for calculating the amount of absorbed energy are described in Sect. 2. Numerical demonstrations to validate the proposed methodology are carried out in Sect. 3. The absorbed energy distribution and its total amount in detailed human head models are derived in Sect. 4 and conclusions are drawn in Sect. 5.

2. Proposed Methodology

2.1 Extraction of Debye Terms from Cole–Cole Model

All materials are assumed to be biological tissues having a complex relative permittivity represented by four Cole–Cole relaxation terms as

$$\varepsilon_r(\omega) = \varepsilon_{r\infty} + \frac{\sigma}{j\omega\varepsilon_0} + \sum_{i=1}^{4} \chi_i(\omega) \tag{1}$$

where

$$\chi_i(\omega) = \frac{\Delta\chi_i}{1 + (j\omega\tau_i)^{1-\alpha_i}} \tag{2}$$

represents the electric susceptibility of the ith relaxation. $\varepsilon_{r\infty}$ and σ are the relative permittivity at an infinite frequency and the conductivity, respectively. ε_0 is the free-space permittivity. $\Delta\chi_i$ denotes the change in the relative permittivity due to the ith relaxation. τ_i is the characteristic relaxation time, and α_i is a parameter determining the broadness of the ith relaxation. To extract Debye parameters of the Cole–Cole model, we first modify the frequency-domain electric susceptibility to that in the complex frequency domain by substituting $j\omega$ with the complex frequency variable s. Then it is numerically transformed into the time-domain impulse response by the FILT [21], [36]. The parameter of the impulse response in the z-domain is finally extracted using the Prony method. For the Cole–Cole relaxation, it was found that the electric susceptibility represented by (2) can be written as a sum of the Debye relaxations, which can be expressed in the z-domain as

$$\chi_i(z) = \sum_{l=1}^{N_i} \frac{A_l^{(i)}}{1 - p_l^{(i)} z^{-1}} \tag{3}$$

where N_i is the number of real poles for the ith relaxation (i = 1, 2, 3, or 4). Note that the number of real poles may be different for each relaxation term. $A_l^{(i)}$ and $p_l^{(i)}$ are the coefficients for each Debye pole determined directly from partial fraction expansion of the z-domain impulse responses. Note that (3) is a monotonically decreasing function in the time domain and, therefore, may be expressed by a sum of Debye terms. The time-domain impulse responses of the Cole–Cole model are determined as

$$\chi_i(t) = \sum_{l=1}^{N_i} \frac{\Delta\chi_l^{(i)}}{\tau_l^{(i)}} \exp\left(-\frac{t}{\tau_l^{(i)}}\right) \tag{4}$$

where $\Delta\chi_l^{(i)}$ and $\tau_l^{(i)}$ are the Debye parameters which are related to the coefficients $A_l^{(i)}$ and $p_l^{(i)}$ as follows [37]:

$$\tau_l^{(i)} = -\frac{\Delta t}{\ln p_l^{(i)}} \tag{5}$$

$$\Delta\chi_l^{(i)} = \frac{A_l^{(i)}\tau_l^{(i)}}{\Delta t} = -\frac{A_l^{(i)}}{\ln p_l^{(i)}} \tag{6}$$

where Δt denotes the time step interval used in the normalization of the relaxation time τ_i when applying the FILT to (2). The expression in the frequency domain is then determined as

$$\chi_i(\omega) = \sum_{l=1}^{N_i} \frac{\Delta\chi_l^{(i)}}{1 + j\omega\tau_l^{(i)}}. \tag{7}$$

The Cole–Cole model is now transformed into a sum of Debye models in the frequency domain. It should be noted that (7) can now be formulated using conventional recursive convolution (RC) techniques, ADE method, or the z-transformation and the time step interval in the FDTD formulation can now be chosen arbitrarily.

2.2 Formulation of Frequency-Dependent FDTD Method Using Auxiliary Differential Equation Method

Electromagnetic fields in isotropic media are described in the frequency domain by Maxwell's equations as

$$\nabla \times \mathbf{H}(\omega) = j\omega\varepsilon_0\hat{\varepsilon}_r(\omega)\mathbf{E}(\omega) \tag{8}$$

$$\nabla \times \mathbf{E}(\omega) = -j\omega\mu\mathbf{H}(\omega) \tag{9}$$

where $\mathbf{E}(\omega)$ and $\mathbf{H}(\omega)$ are the time-harmonic electric and magnetic fields, respectively. μ is the permeability, ε_0 is the permittivity in free space, and $\hat{\varepsilon}_r(\omega)$ is the complex relative permittivity, which is expressed as (1) for biological tissues. Substituting (1) into (8) gives

$$\nabla\times\mathbf{H}(\omega) = j\omega\varepsilon_0\left(\varepsilon_{r\infty} + \frac{\sigma}{j\omega\varepsilon_0} + \sum_{i=1}^{4}\chi_i(\omega)\right)\mathbf{E}(\omega). \tag{10}$$

Each Cole–Cole term can be transformed into multiple Debye terms as (7), therefore, (10) is expressed as

$$\nabla \times \mathbf{H}(\omega) = j\omega\varepsilon_0\varepsilon_{r\infty}\mathbf{E}(\omega) + \sigma\mathbf{E}(\omega) + \sum_{l=1}^{N_l}\mathbf{J}_l(\omega) \tag{11}$$

where the nested sums of Debye terms are merged into a single summation, $N_l = N_1+N_2+N_3+N_4$ is the total number of Debye terms contributed from the four Cole–Cole relaxation terms, and

$$\mathbf{J}_l(\omega) = \frac{j\omega\varepsilon_0\Delta\chi_l}{1 + j\omega\tau_l}\mathbf{E}(\omega) \tag{12}$$

represents the polarization current density for each Debye term. By taking the inverse Fourier transform of (12), we obtain the differential equation describing the relationship between $\mathbf{E}$ and $\mathbf{J}_l$ as

$$\tau_l\frac{\partial\mathbf{J}_l(t)}{\partial t} + \mathbf{J}_l(t) = \varepsilon_0\Delta\chi_l\frac{\partial\mathbf{E}(\omega)}{\partial t}. \tag{13}$$

The above equation is then discretized using the central difference method at the time step $t = (n-1/2)\Delta t$ and the update equation for $\mathbf{J}_l$ is obtained as

$$\mathbf{J}_l^n = q_l\mathbf{J}_l^{n-1} + B_l\left(\mathbf{E}^n - \mathbf{E}^{n-1}\right) \tag{14}$$

where

$$q_l = \frac{1-\frac{\Delta t}{2\tau_l}}{1+\frac{\Delta t}{2\tau_l}}, B_l = \frac{\varepsilon_0\Delta\chi_l}{\tau_l}\frac{1}{1+\frac{\Delta t}{2\tau_l}}. \tag{15}$$

Transforming (11) into its time-domain expression and applying the central difference at the same time step $t = (n-1/2)\Delta t$ gives

$$\frac{\Delta t}{\varepsilon_0}\nabla\times\mathbf{H}|^{n-\frac{1}{2}} = \left(\varepsilon_{r\infty} + \frac{\sigma\Delta t}{2\varepsilon_0}\right)\mathbf{E}^n - \left(\varepsilon_{r\infty} - \frac{\sigma\Delta t}{2\varepsilon_0}\right)\mathbf{E}^{n-1} + \frac{\Delta t}{\varepsilon_0}\sum_{l=1}^{N_l}\frac{\mathbf{J}_l^n + \mathbf{J}_l^{n-1}}{2}. \tag{16}$$

By substituting (14) into (16), the update equation for the electric field is formulated as

$$\mathbf{E}^n = \frac{1}{K_0}\left[G_0\mathbf{E}^{n-1} - \sum_{l=1}^{N_l}(1+q_l)\mathbf{J}_l'^{,n-1} + \Delta t\nabla\times\mathbf{H}^{n-\frac{1}{2}}\right] \tag{17}$$

where,

$$\mathbf{J}_l'^{,n} = q_l\mathbf{J}_l'^{,n-1} + B_l'\left(\mathbf{E}^n - \mathbf{E}^{n-1}\right) \tag{18}$$

$$K_0 = \varepsilon_{r\infty} + \frac{\sigma\Delta t}{2\varepsilon_0} + \sum_{l=1}^{N_l}B_l' \tag{19}$$

$$G_0 = \varepsilon_{r\infty} - \frac{\sigma\Delta t}{2\varepsilon_0} + \sum_{l=1}^{N_l}B_l' \tag{20}$$

$$B_l' = \frac{\Delta\chi_l\Delta t}{2\tau_l + \Delta t}. \tag{21}$$

Note that $\mathbf{J}_l = \Delta t/(2\varepsilon_0)\mathbf{J}_l'$ is applied here to simplify the formulation.

2.3 Calculation of Specific Energy Absorption

The terms used in this study for different physical quantities are defined as follows:

- SA : Specific energy absorption in J/kg, representing the cumulative amount of energy absorbed into a tissue per unit mass [38].
- SA_{L} : Specific energy loss in J/kg, representing the per-mass cumulative energy loss through dissipation into a tissue, which is transformed into heat [39]
- P_{E} : Transient electric power density in W/m^3, which indicates the density of electric energy into a tissue per unit time. Note that the electric energy may exhibit a negative value when an excessive release of energy occurs
- P_{L} : Transient power loss density in W/m^3, which represents the power dissipated into a tissue per unit volume [40]. Note that only a positive value is allowed for P_{L} since it represents a real loss in the medium

Firstly, SA is calculated using FDTD simulations with the following equations [31], [38]:

$$SA = \frac{1}{\rho}\int_0^{T_{\max}}\mathbf{E}(t)\cdot\frac{\partial\mathbf{D}(t)}{\partial t}dt \approx \frac{\Delta t}{\rho}\sum_{n=1}^{N\Delta t}P_{\mathrm{E}}^{n-1/2} \tag{22}$$

where

$$P_{\mathrm{E}}^{n-1/2} = \frac{1}{2\Delta t}\left(\mathbf{E}^n + \mathbf{E}^{n-1}\right)\cdot\left(\mathbf{D}^n - \mathbf{D}^{n-1}\right) \tag{23}$$

and ρ is the mass density of biological tissues. As the explicit physical interpretation, P_{E} represents the sum of two physically distinct quantities: one that represents the power density dissipated into the medium in the form of heat and one that presents the sum of the power density stored in the

field and the reactively stored power density in the medium [41]. Therefore, P_{E} may exhibit a negative value due to an excessive release of the stored energy at a certain time. However, when the reactive electric energy deceases over a long calculation time after the EM pulse vanishes, SA will eventually reach the same value as the real energy loss SA_{L} as will be shown later in our numerical results. Meanwhile, P_{L} represents only the power density loss in the medium which is transformed into heat. To derive SA_{L} and P_{L} in a medium, we employ the equivalent circuit (EC) approach in the FDTD formulation as in [39], [42]. Since (11) can be considered as an EC in Fig. 1, the electrical parameter values per unit length of the lumped elements are derived as

$$G_0 = \sigma, C_0 = \varepsilon_0 \varepsilon_{r\infty} \tag{24}$$

$$R_l = \frac{\tau_l}{\varepsilon_0 \Delta\chi_l}, C_l = \varepsilon_0 \Delta\chi_l. \tag{25}$$

The total current density in the time-domain is expressed as

$$\mathbf{J}(t) = \mathbf{J}_C(t) + \mathbf{J}_G(t) + \sum_{l=1}^{N_l} \mathbf{J}_l(t) \tag{26}$$

where $\mathbf{J}_C(t) = C_0 \frac{\partial \mathbf{E}(t)}{\partial t}$, $\mathbf{J}_G(t) = G_0 \mathbf{E}(t)$, and $\mathbf{J}_l(t)$ is the current density flowing into the RC branches as shown in Fig. 1. Each branch corresponds to a Debye relaxation term whose parameters are extracted using the proposed parameter extraction method described in Sect. 2.1. Therefore, the power loss densities for the lumped resistances R_l and parallel conductance G_0 in Fig. 1 are calculated using

$$P_{R_l}(t) = R_l \mathbf{J}_l(t) \cdot \mathbf{J}_l^*(t) \tag{27}$$

$$P_{G_0}(t) = \frac{1}{G_0} \mathbf{J}_G(t) \cdot \mathbf{J}_G^*(t). \tag{28}$$

The power loss density due to the lumped resistances R_l and parallel conductance G_0 at a discrete time can be determined as

$$P_{R_l}^n = \frac{\tau_l}{\varepsilon_0 \Delta\chi_l} \mathbf{J}_l^n \cdot \left(\mathbf{J}_l^n\right)^* = \frac{4\varepsilon_0 \tau_l}{\Delta t^2 \Delta\chi_l} \left|\mathbf{J}_l'^{,n}\right|^2 \tag{29}$$

$$P_{G_0}^n = \sigma \left|\mathbf{E}^n\right|^2 \tag{30}$$

respectively. Finally, SA_{L} is expressed as

$$SA_L = \frac{1}{\rho} \int_0^{T_{\max}} \left[P_{G_0}(t) + P_{R_l}(t)\right] dt \approx \frac{\Delta t}{\rho} \sum_{n=1}^{N\Delta t} P_{\mathrm{L}}^{n-1/2} \tag{31}$$

where

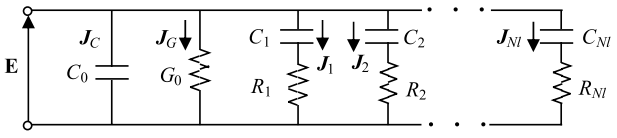

Fig. 1 Equivalent circuit of Cole–Cole model.

$$P_{\mathrm{L}}^{n-1/2} = \sigma \left|\mathbf{E}^{n-1/2}\right|^2 + \frac{1}{\varepsilon_0} \sum_{l=1}^{N_l} \frac{\tau_l}{\Delta\chi_l} \left|\mathbf{J}_l^{n-1/2}\right|^2 \tag{32}$$

represents the transient specific power loss density at the $(n-1/2)$th time step. Note that the electric field and current density at the $(n-1/2)$th time step are determined by averaging of those at the nth and $(n-1)$th time steps. SA_{L} is the only term to be considered when calculating the temperature rise since it represents the absorbed energy that is transformed into heat. The SAR in W/kg at a discrete time step can also be calculated from SA_{L} as

$$\left.\frac{\partial SA_{\mathrm{L}}(\mathbf{r},t)}{\partial t}\right|^{t=\left(n-\frac{1}{2}\right)\Delta t} \approx \frac{P_{\mathrm{L}}^{n-\frac{1}{2}}}{\rho} = \mathrm{SAR}^{n-\frac{1}{2}}. \tag{33}$$

3. Numerical Validation

3.1 Determination of Debye Parameters from Cole–Cole Model

To begin with, we investigate the validity of the proposed formulations for Debye relaxation expressed by (2) having parameters of $\Delta\chi_1 = 3.0$, $\tau_1 = 64$ ps, and $\alpha_1 = 0$. Time step interval is set to $\Delta t = 3.85$ ps. After applying the FILT to (2) with the relaxation time normalized by Δt, the impulse response sequence is determined at $n = 0.5, 1.5, 2.5, \ldots,$ 4000.5 since we cannot directly obtain the result at $n = 0$ using the FILT. The maximum number of terms required to satisfy an accuracy of 10^{-5} in the time-domain impulse response is 1179 when $n = 4000.5$. The Prony method is then applied to derive the coefficients A_1 and p_1 with an allowable error of 10^{-5}. Note that the extracted coefficients A_1 and p_1 are for $n = 0.5$. However, A_1 and p_1 at $n = 0$ are required for the parameter extraction to determine the Debye parameters by (5) and (6). Here we use the following equations to approximate the coefficients A_1 and p_1 at $n = 0$:

$$A_l^{(0)} = \frac{A_l^{(0.5)}}{\sqrt{p_l^{(0.5)}}}, p_l^{(0)} = p_l^{(0.5)} \tag{34}$$

where $A_l^{(0.5)}$ and $p_l^{(0.5)}$ are the residues and poles derived from the impulse response sequence at $n = 0.5, 1.5, 2.5, \ldots, 4000.5$, respectively. The superscript indicates the start time step index of the impulse response sequence which is $n = 0.5$ in our study. Using (5) and (6), we then obtain $\Delta\chi_1 = 2.99999$ and $\tau_1 = 64.0025$ ps, which are almost identical to the exact values of $\Delta\chi_1 = 3.0$, $\tau_1 = 64$ ps. Therefore, the validity of our extraction method has been demonstrated.

Next, we adopt our Debye parameter extraction method to the Cole–Cole model of muscle. The Cole–Cole parameters are extracted from Gabriel's database [20]. Using the same procedures as above, we obtain the residues A_l and poles p_l as tabulated in Table 1. Numbers of coefficients are determined to be 8, 12, and 12 for the first, second, and third Cole–Cole relaxation terms, respectively, with an allowable error of 10^{-5}. The extracted parameters are also shown in

Table 1 Extracted Debye parameters for the Cole–Cole models.

	Determined coefficients	Extracted parameters (f_l in GHz)
1st term	$A_1 = 6.96198, p_1 = 0.49350$	$\Delta\chi_1 = 14.033, f_1 = 183.36$
	$A_2 = 6.82613, p_2 = 0.62870$	$\Delta\chi_2 = 18.550, f_2 = 120.50$
	$A_3 = 2.88101, p_3 = 0.30103$	$\Delta\chi_3 = 4.3738, f_3 = 311.69$
	$A_4 = 1.59396, p_4 = 0.75867$	$\Delta\chi_4 = 6.6259, f_4 = 71.707$
	$A_5 = 1.25497, p_5 = 0.10192$	$\Delta\chi_5 = 1.7214, f_5 = 592.87$
	$A_6 = 0.27976, p_6 = 0.87280$	$\Delta\chi_6 = 2.2011, f_6 = 35.322$
	$A_7 = 0.04555, p_7 = 0.94877$	$\Delta\chi_7 = 0.88926, f_7 = 13.654$
	$A_8 = 0.00415, p_8 = 0.98790$	$\Delta\chi_8 = 0.34251, f_8 = 3.1616$
2nd term	$A_9 = 0.11212, p_9 = 0.99995$	$\Delta\chi_9 = 2205.6, f_9 = 0.0132$
	$A_{10} = 0.02828, p_{10} = 0.99781$	$\Delta\chi_{10} = 12.892, f_{10} = 0.5701$
	$A_{11} = 0.02035, p_{11} = 0.98797$	$\Delta\chi_{11} = 1.6922, f_{11} = 3.1416$
	$A_{12} = 0.01591, p_{12} = 0.96316$	$\Delta\chi_{12} = 0.43201, f_{12} = 9.7452$
	$A_{13} = 0.01302, p_{13} = 0.91690$	$\Delta\chi_{13} = 0.15676, f_{13} = 22.523$
	$A_{14} = 0.01095, p_{14} = 0.84455$	$\Delta\chi_{14} = 0.07050, f_{14} = 43.863$
	$A_{15} = 0.00934, p_{15} = 0.74407$	$\Delta\chi_{15} = 0.03663, f_{15} = 76.752$
	$A_{16} = 0.00802, p_{16} = 0.61678$	$\Delta\chi_{16} = 0.02114, f_{16} = 125.47$
	$A_{17} = 0.00687, p_{17} = 0.46829$	$\Delta\chi_{17} = 0.01323, f_{17} = 196.97$
	$A_{18} = 0.00578, p_{18} = 0.30993$	$\Delta\chi_{18} = 0.00886, f_{18} = 304.13$
	$A_{19} = 0.00464, p_{19} = 0.16066$	$\Delta\chi_{19} = 0.00634, f_{19} = 474.72$
	$A_{20} = 0.00337, p_{20} = 0.04740$	$\Delta\chi_{20} = 0.00508, f_{20} = 791.63$
3rd term	$A_{21} = 0.04235, p_{21} = 0.99997$	$\Delta\chi_{21} = 1215.2, f_{21} = 0.0090$
	$A_{22} = 0.01049, p_{22} = 0.99781$	$\Delta\chi_{22} = 4.7917, f_{22} = 0.5688$
	$A_{23} = 0.00763, p_{23} = 0.98798$	$\Delta\chi_{23} = 0.63461, f_{23} = 3.1404$
	$A_{24} = 0.00598, p_{24} = 0.96317$	$\Delta\chi_{24} = 0.16231, f_{24} = 9.7436$
	$A_{25} = 0.00489, p_{25} = 0.91691$	$\Delta\chi_{25} = 0.05893, f_{25} = 22.522$
	$A_{26} = 0.00412, p_{26} = 0.84455$	$\Delta\chi_{26} = 0.02651, f_{26} = 43.863$
	$A_{27} = 0.00351, p_{27} = 0.74406$	$\Delta\chi_{27} = 0.01377, f_{27} = 76.755$
	$A_{28} = 0.00302, p_{28} = 0.61676$	$\Delta\chi_{28} = 0.00795, f_{28} = 125.47$
	$A_{29} = 0.00258, p_{29} = 0.46826$	$\Delta\chi_{29} = 0.00497, f_{29} = 196.99$
	$A_{30} = 0.00217, p_{30} = 0.30991$	$\Delta\chi_{30} = 0.00333, f_{30} = 304.15$
	$A_{31} = 0.00175, p_{31} = 0.16065$	$\Delta\chi_{31} = 0.00238, f_{31} = 474.74$
	$A_{32} = 0.00127, p_{32} = 0.04740$	$\Delta\chi_{32} = 0.00191, f_{32} = 791.66$

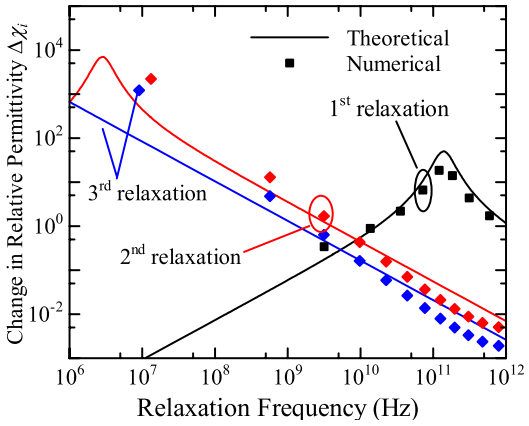

Fig. 2 Debye parameters retrieved from Cole–Cole models of muscle.

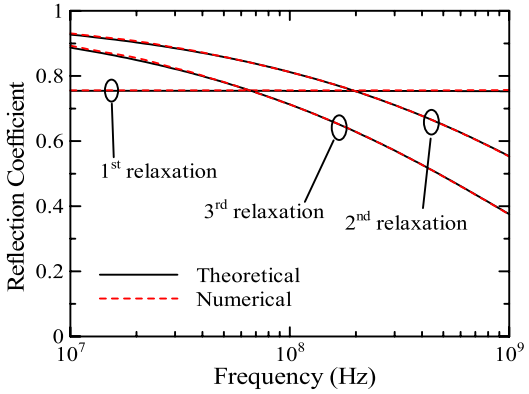

Fig. 3 Reflection coefficients obtained from theory and numerically derived using the extracted Debye parameters for each Cole–Cole term.

Table 1 and plotted in Fig. 2, along with their theoretical values in solid black lines, which are determined from (7) of [43]. Each point indicates the relaxation frequency and corresponding $\Delta\chi_i$ of the Debye model in (7). The relaxation frequency is calculated using $f_l = 1/\tau_l$, where τ_l denotes the relaxation time of each Debye term. The parameters extracted using our proposed method are in fair agreement with the theoretical values. After the parameters are extracted, we perform numerical simulations to calculate the reflection coefficient of each Cole–Cole term of the medium. The one-dimensional model used therein is the same as that in [34]. The total number of cells is 5016, including the convolutional perfectly matched layers (CPMLs) [44]. The Eight-layer CPMLs are utilized to truncate the analysis domain at both sides to absorb the outgoing EM waves. The cell size is chosen to be 2 mm. The incident wave expressed by a Gaussian waveform as

$$E^{\text{inc}}(t) = \exp\left(-\left(\frac{t - T_0}{\alpha_0}\right)^2\right), \tag{35}$$

where $T_0 = 0.385$ ns and $\alpha_0 = 0.194$ ns, is used as a source. The applied pulse contains broad frequency components from dc to approximately 5 GHz. Figure 3 shows the reflection coefficients derived using the extracted parameters and those calculated using the method in [31]. The reflection coefficient is calculated using the following equation:

$$\Gamma(\omega) = \left|\frac{1 - \sqrt{1 + \chi_i(\omega)}}{1 + \sqrt{1 + \chi_i(\omega)}}\right|, \tag{36}$$

where χ_i is the Cole-Cole electric susceptibility expressed in (2). The results for all Cole–Cole terms show good agreement with theoretical values, confirming the validity of the method. Errors in the reflection coefficients when compared with theoretical values are also calculated and depicted as a solid black line in Fig. 4. The errors for the proposed method are less than 0.3% over a broad frequency range from 10 MHz to 1 GHz. The errors match those derived by the method in [31] up to around 100 MHz whereas we can see an increase in the errors at higher frequencies over 200 MHz. The increase may be due to the difference in the update equation of the auxiliary current density in (14), which has second-order accuracy for both time and space, whereas that of [31] has only first-order accuracy in the space of the electric field and, therefore, the difference is larger at higher frequencies.

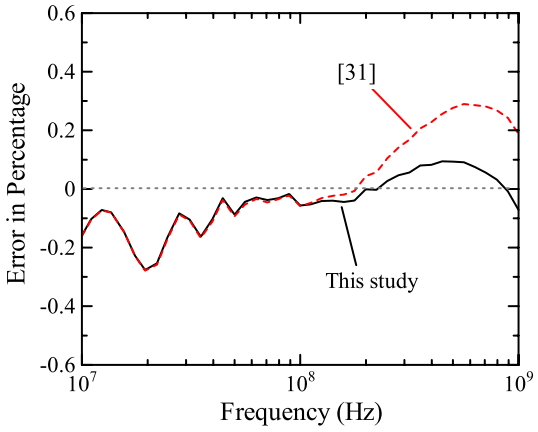

Fig. 4 Errors in reflection coefficients obtained using the extracted Debye parameters for four-term Cole–Cole model of muscle and those in [31].

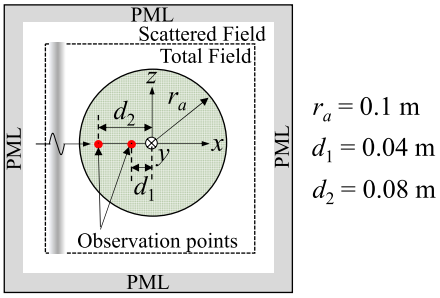

Fig. 5 3-D analysis domain of homogeneous dielectric sphere of muscle and locations of observation points.

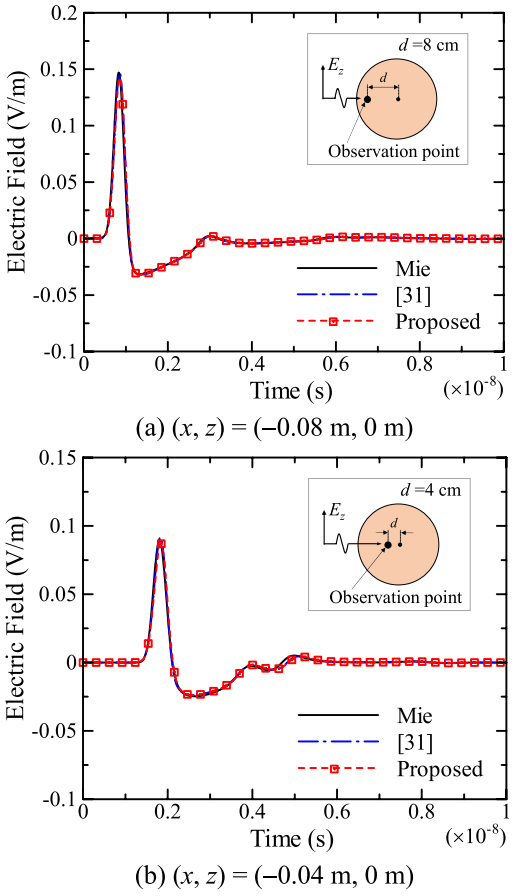

Fig. 6 Electric field at observation points in comparison with the FDTD method in [31] and those obtained by Mie theory.

3.2 Energy Deposition into Homogeneous Dielectric Sphere

To demonstrate the validity of the proposed FDTD scheme, numerical analyses of the electric field waveform and the specific power loss dissipated into a homogeneous dielectric sphere having dielectric properties represented by four Cole–Cole relaxation terms are calculated and compared with analytical results obtained from Mie theory [45]. Figure 5 illustrates the analysis model of the homogeneous dielectric sphere of the muscle tissue. The origin of the coordinates coincides with the center of the sphere. The radius of the sphere is $r_a = 0.1$ m. The number of coefficients for muscle is 33 when an allowable error of 10^{-5} is chosen. An EM planewave with polarization in the z-direction impinges into the sphere from the $-x$-direction. The amplitude of the incident electric field is 1 V/m. The waveform of the incident electric field is the Gaussian pulse with $T_0 = 0.385$ ns and $\alpha_0 = 0.146$ ns. The spatial resolution and time step for the FDTD calculation are 2 mm and $\Delta t = 3.85$ ps, respectively. The total number of cells in analysis model is $141 \times 141 \times 141$. Eight-layered PMLs are placed outside the analysis region to absorb the outgoing EM waves. The number of calculation time steps is 5000. All numerical analyses are performed on a workstation (Intel Xeon E5-2697v3 @ 2.6 GHz, 512-GB memory) with 22 parallel threads. The calculation time is approximately 320 s.

Figures 6(a) and (b) show the time-domain electric field calculated at two observation locations $(x, z) = (-0.08\,\text{m}, 0\,\text{m})$ and $(-0.04\,\text{m}, 0\,\text{m})$ with respect to the center of the sphere, respectively, as shown in Fig. 5. The Mie solutions are calculated by the inverse Fourier transform of those in the frequency domain [45]. Note that the Mie solutions cannot be obtained at the center of the sphere due to the divergence of the Hankel function with zero argument. As seen from Figs. 6(a) and (b), the time-domain electric fields derived by the proposed FDTD method agree well with the analytical Mie solutions in the time domain, demonstrating the validity of our proposed method. They also exactly match the numerical simulation results, shown as the dash-dotted blue lines, obtained by the FDTD method described in [31]. The amplitude of the pulse decreases as it advances into the dielectric sphere. From Fig 6(b), we observe small differences in the late-time response at around 4.8 ns. The differences are attributed from errors in modeling the sphere using the staggered grid of the FDTD method. The EM wave travelling along the curved sphere surface will take a longer time to reach the back of the sphere in numerical simulations since the staircase approximation of

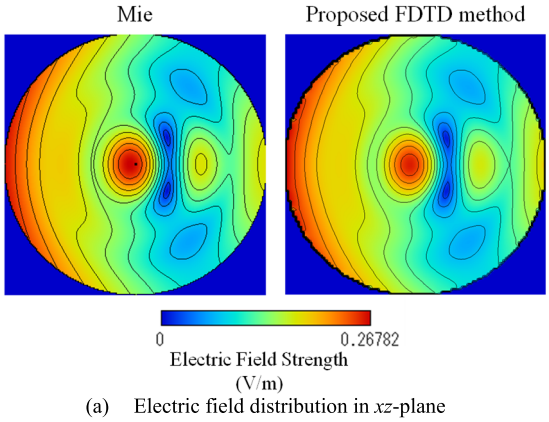

(a) Electric field distribution in *xz*-plane

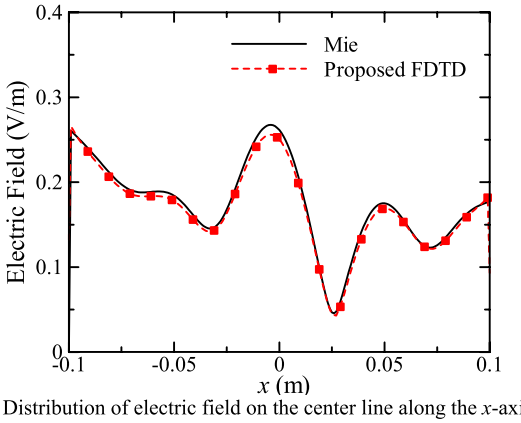

(b) Distribution of electric field on the center line along the *x*-axis

Fig. 7 Electric field distributions inside the homogeneous dielectric sphere of muscle at 500 MHz.

the sphere boundary results in the increased travel distance of EM pulses. The effect seems to be smaller for the location $(x, z) = (-0.08\,\text{m}, 0\,\text{m})$ in Fig. 6(a), since most of the diffracted EM wave energy penetrating the sphere from the back is absorbed and cannot reach the front of the sphere where the observation point is located. It is also observed that the pulse penetrating the sphere is oscillatory and has both positive and negative values even though the incident electric field has only positive values.

Figure 7(a) and (b) shows the electric field distribution inside the homogeneous muscle sphere characterized by four Cole–Cole terms at 500 MHz using the on-the-fly Fourier transform with a single FDTD run and that obtained from Mie theory. As can be seen from the figure, the result obtained by the proposed FDTD method is in good agreement with the Mie solution, demonstrating the validity of the method. A strong electric field appears not only close to the surface but also near the center of the sphere with the peak shifted to an anterior location due to the concentration of the EM wave penetrating the sphere. The increased absorption is due to a combination of high dielectric constant and the curvature of the sphere. The result shows a similar trend to those in the literature [46]. Although not shown here, it is noteworthy that the electric field distributions, obtained using the extracted parameters, at other frequencies in the valid range between 10 MHz and 1 GHz are also in

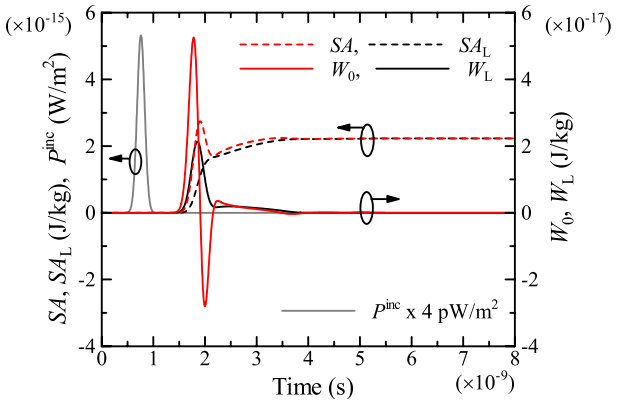

Fig. 8 Transient specific energy absorption and specific energy loss for an incident Gaussian pulse of 1 V/m.

good agreement with the analytical Mie results.

Figure 8 shows SA, SA_{L}, W_0, and W_{L} with respect to time at $(x, z) = (-0.04\,\text{m}, 0\,\text{m})$, where W_0 and W_{L}, calculated using

$$W_0 = \frac{\Delta t}{\rho} P_E, W_L = \frac{\Delta t}{\rho} P_L \tag{37}$$

are the transient specific energy absorption and transient specific energy loss, respectively. They represent the energy that is stored or dissipated into the medium over a single time step. Incident power density of the Gaussian pulse with a full width at half maximum (FWHM) of approximately 0.172 ns is also indicated as a grey solid line in Fig. 8. As shown in the figure, W_0 shows greater variation than W_{L}, which is the energy loss by dissipation into the medium. It is clearly observed that W_0 exhibits a negative value at around 2 ns due to the excessive release of stored energy while W_{L} only takes positive values. It is seen that FWHM of W_L is approximately 0.280 ns, wider than that of incident power density due to dispersive nature of Cole–Cole model. As might be expected, while SA may decrease due to the release of stored energy, SA_{L} monotonically increases to a specific value, which indicates the total amount of specific energy loss within a single cycle of the EM pulse. At the end of the pulse illumination, both SA and SA_{L} reach the same value of the specific energy absorption after the EM pulse diminishes to zero or after 5 ns as shown in Fig. 8. Figure 9 depicts the SA distribution of the muscle sphere in the xz plane. SA is calculated until the EM pulse amplitude deceases to a negligible level at the 10000th time step. The figure shows that the highest peak of SA appears at the surface of the sphere. There are two other peaks, which appear near but not exactly at the center of the sphere. The shift in the location of the SA peaks is attributed to the transmission properties caused by high dielectric constants of the medium and the refraction of the incident plane wave propagating along the curved surface. The maximum value of SA is 1.062×10^{-14} J/kg, almost the same as 1.038×10^{-14} J/kg, the SA maximum derived in [31]. The difference in the maximum SA between the two methods is approximately 2.26%. The difference is

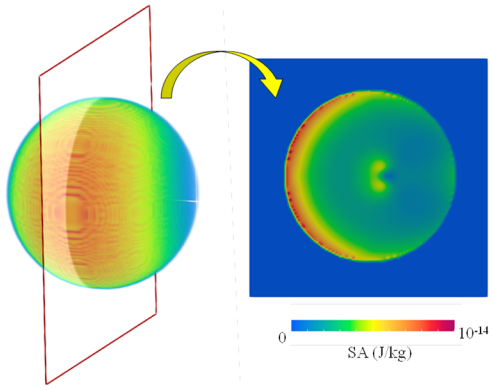

Fig. 9 Specific energy absorption SA of Gaussian EM pulse having an incident electric field strength of 1 V/m.

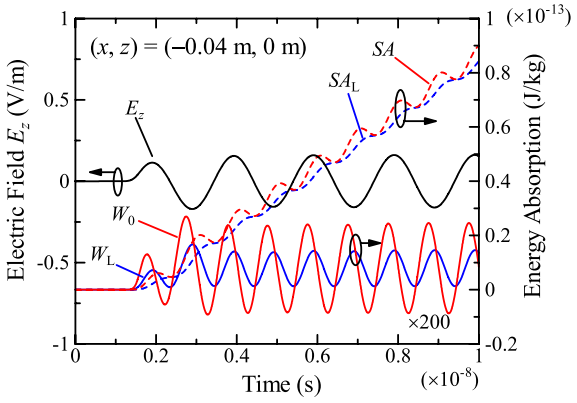

Fig. 10 Electric field E_z and energy absorptions (SA, SA_{L}, W_0, W_{L}) at an observation point located at $(x, z) = (-0.04\,\mathrm{m}, 0\,\mathrm{m})$.

caused by the different formulation of the Debye terms as mentioned in Sect. 3.1.

To further confirm the correctness of the proposed algorithm for determining the specific energy absorption and specific energy loss, we apply a sinusoidal waveform oscillating at 500 MHz as an incident plane wave to the same sphere model. Figure 10 shows the electric field E_z and the specific energy absorptions SA, SA_{L}, W_0, and W_{L} at the observation point $(x, z) = (-0.04\,\mathrm{m}, 0\,\mathrm{m})$. It is interesting that both W_0 and W_{L} oscillate at a higher frequency of 1 GHz, twice that of the electric field at the same point. It can also be observed in the figure that W_0 may exhibit a negative value, indicating the excessive release of the stored energy. Meanwhile, W_{L} shows only positive values. To compare these results with analytical solutions, we calculate the SAR over a period of the analysis frequency using the following equations derived from (33) and (37):

$$\mathrm{SAR}(k) = \frac{1}{\rho T_0}\int_{kT_0}^{(k+1)T_0} P_L(t)dt = \frac{1}{T_0}\sum_{i=kT_0/\Delta t}^{(k+1)T_0/\Delta t} W_L^i \tag{38}$$

where $kT_0 \le i\Delta t \le (k+1)T_0$, T_0 is the time period, and k is the index number of the period. Figure 11 shows the specific

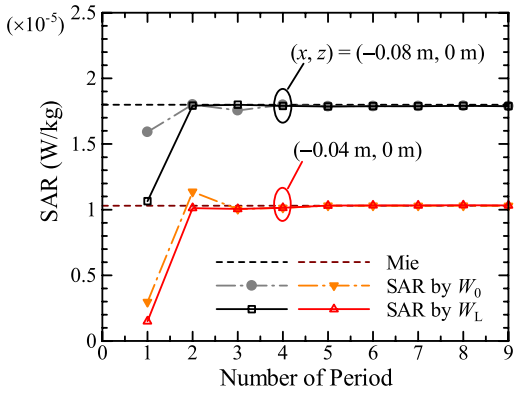

Fig. 11 Specific absorption rate for an incident field at 500 MHz.

absorption rates calculated using W_{L} or W_0 in (38) at the observation points $(x, z) = (-0.08\,\mathrm{m}, 0\,\mathrm{m})$ and $(-0.04\,\mathrm{m}, 0\,\mathrm{m})$. The theoretical values are determined from

$$\mathrm{SAR}^{\mathrm{Mie}} = \frac{\sigma\left|\mathbf{E}^{\mathrm{Mie}}\right|^2}{2\rho} \tag{39}$$

where $\mathbf{E}^{\mathrm{Mie}}$ is the electric field strength obtained from Mie theory. Specific absorption rates $\mathrm{SAR}^{\mathrm{Mie}}$ are also indicated in Fig. 11 as the dashed lines. As can be seen from Fig. 11, SARs calculated using either W_0 or W_{L} closely matched with the Mie solutions when the EM waves reach their steady state after five periods, demonstrating the correctness of the expressions for calculating the SAs in (22) and (31). Therefore, the average values of W_0 and W_{L} over a period are the same. W_0 and W_{L} at times of less than five periods are in a transient stage, resulting in differences from the theory. It should be emphasized that for the sinusoidal sources, the average values of both W_0 and W_{L} match each other in the steady state but they will be different for a pulse waveform, where the steady state is not sustained. From the physical meanings of W_0 and W_{L}, it is worth mentioning that W_{L} should be the only quantity used as a heat source when calculating the temperature elevation due to the exposure of EM pulses.

4. EM Pulse Exposure to Human Head

4.1 Human Head Models and Analysis Parameters

To calculate the EM energy deposition into a human head, numerical human head models are extracted from the Japanese adult male and female models TARO and HANAKO, respectively, which were developed by the National Institute of Information and Communications Technology, Tokyo, Japan [47]. Figure 12 illustrates the head models, which comprise of 26 different tissues and organs with a resolution of 2 mm. The dielectric properties of biological tissues are represented by the four-term Cole–Cole model and their Debye parameters are extracted using the proposed parameter extraction method and used in the FDTD simulations. An EM plane wave with a polarization direction in the z-axis and a magnitude of 1 V/m

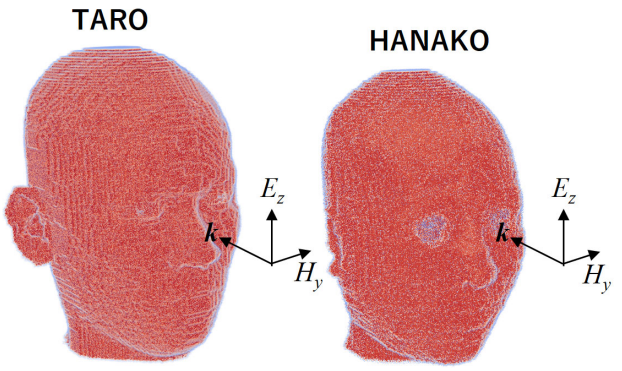

Fig. 12 Numerical human head models TARO and HANAKO used in simulations of EM pulse exposures.

is used to impinge on the head models from the front as shown in Fig. 12. The incident pulse used is the Gaussian waveform expressed by (35) with the parameter values of $T_0 = 0.385$ ns and $\alpha_0 = 0.146$ ns. The time step interval is 3.84 ps and the total size of the analysis models with eight-layer PMLs is $166 \times 156 \times 172$ cells for both models. The total computation time for TARO and HANAKO models are 759 s (12 min 39 s) and 750 s (12 min 30 s) for 10,000 time steps, respectively.

4.2 Energy Deposition of EM Planewave into Human Head

The specific energy loss is calculated at each time step using the extracted parameters of the Cole–Cole models. Figure 13(a)–(e) illustrate the calculated transient specific energy loss using (32) and (37) at 100, 150, 200, 250, and 300 steps, respectively. In Fig. 13(a), the EM pulse first reaches the human nose from the front and, hence, the energy is absorbed instantaneously. At 150 steps (Fig. 13(b)), the pulse illuminates the whole face and begins to penetrate the head, resulting in high energy absorption between the eyes, around the eyes, and at the tip of the nose. At 200 steps (Fig. 13(c)), after the EM pulse precursor reaches the top of the head, the energy absorption of the EM pulse occurs at deeper tissues, and the pulse energy begins to concentrate along the z-axis since the curvature of the head model is larger in the azimuth plane than that in the elevation plane. It is observed that energy absorption in the eyes occurs from this step, with a delay compared with that of other superficial tissues such as skin and fat. After 250 steps, a strip of specific energy loss is observed in the human frontal brain as shown in Fig. 13(d). When the EM pulse precursor completely passes through the human head at around 300 steps, the energy continues to be absorbed at the deeper biological tissues inside the head. As shown in Fig. 13(e), the pulse energy absorption at the deeper tissues almost remains in a strip along the z-axis, and it does not spread across the entire head. The energy absorption in the head is considered negligible after approximately 2000 time steps for the Gaussian pulse used in this study, and the simulations are stopped. By using the proposed ex-

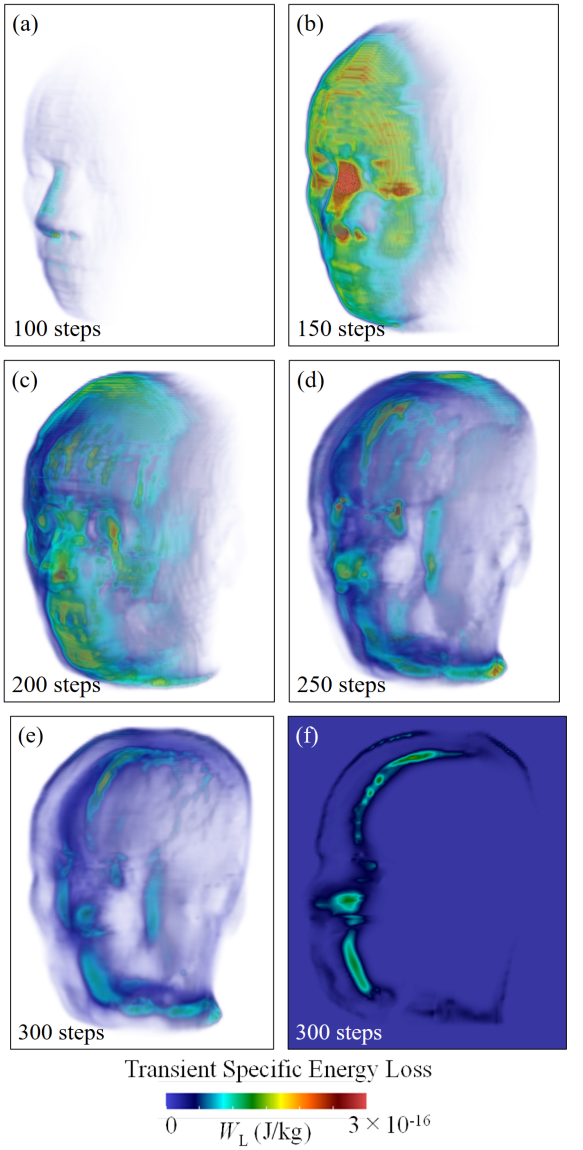

Fig. 13 Distribution of the transient specific energy loss in a human head model at (a) 100, (b) 150, (c) 200, (d) 250, and (e) 300 time steps, and (f) xz-plane distribution of the transient energy loss at 300 time steps.

tracted parameters, for the first time, we can derive the transient specific energy loss at every time steps, which cannot be obtained using the conventional method. Note again that the specific energy loss corresponds to the temperature rise in biological tissues and has physical meanings, while the specific energy absorption includes the stored energy, which may be released over time. Figure 14 indicates the specific energy absorption for the TARO and HANAKO head models. The result for TARO is also consistent with that in [31], demonstrating the validity of the proposed method. As indicated in Fig. 14, *SA* shows higher values at the skin and the tissues just beneath the skin such as muscle. It also shows moderate values in the deep tissues such as the cerebrospinal fluid (CSF) at locations p_1 and p_2, the tongue, and cartilage. *SA* in HANAKO tends to be higher due to the

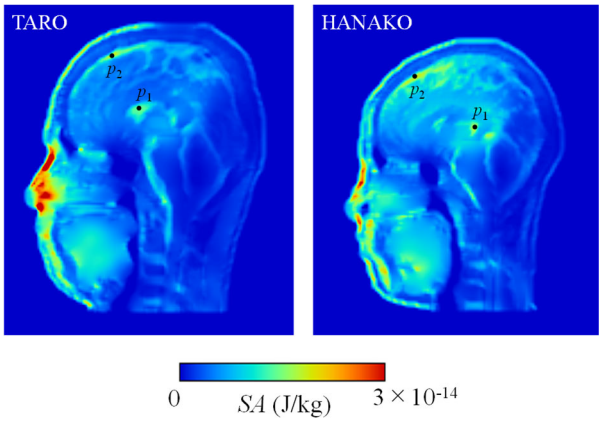

Fig. 14 Specific energy absorption in TARO and HANAKO head model due to a single pulse of illumination.

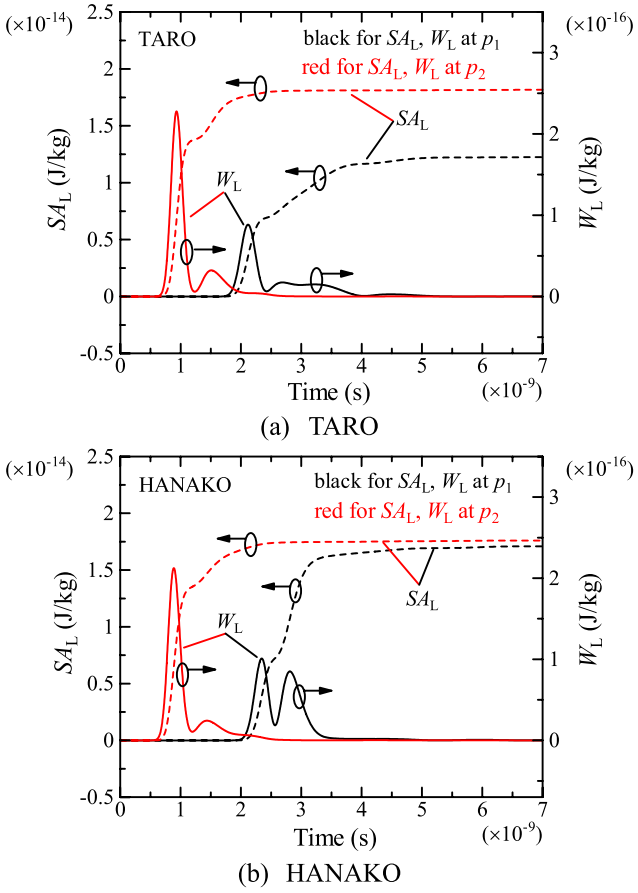

Fig. 15 Specific energy absorption in (a) TARO and (b) HANAKO head models due to a single pulse of illumination.

smaller volume of the head with the larger curvature and the larger portion of CSF than that in TARO. The maximum values of SA in TARO and HANAKO are 5.58×10^{-14} and 4.78×10^{-14} J/kg, respectively. Note that the results of SA obtained here can be used in compliance with international exposure standards [48], [49].

Figures 15(a) and (b) show the specific energy loss and its transient component at two observation points indicated in Fig. 14 as p_1 (CSF) and p_2 (CSF) for TARO and HANAKO, respectively. It is observed that most of the pulse energy is rapidly absorbed into the tissue due to the first incoming pulse which penetrates the head from the front for both p_1 and p_2 in TARO. However, for HANAKO, the same trend only applies at p_2, which is located near the head surface. At the observation point p_1, we observe almost the same energy of the second wave. This is due to the diffraction of the EM pulse around the head. The larger curvature and smaller size of HANAKO model also contribute to higher absorption inside the deep tissues. It should be emphasized that it is very important to take into account the dispersion characteristic in order to quantify correctly amount of absorbed energy or electric/magnetic field strengths inside biological tissues since they are directly related to many biological effects such as body temperature elevation and nervous stimulus. Inaccurate dosimetric results may lead to misinterpretation of biological effects observed in experiments. In conclusion, it has been demonstrated that the numerical method proposed in this paper can fully take into account the frequency dependence of the dielectric properties of biological media, provides accurate dosimetric results, and gives physical insight into the interaction between biological bodies and EM pulses.

5. Conclusion

In this paper, we have proposed a Debye parameter extraction method for the Cole–Cole model, which is used to represent the dielectric properties of biological media. We have also developed a frequency-dependent FDTD method incorporating the parameters extracted via the formulation of the update electric field using the ADE method and we also provided an algorithm for calculating specific energy loss and its transient component, which cannot be determined using the conventional approach. The validity of the parameter extraction method has been demonstrated via comparison between numerical results and those obtained by an analytical method. It was shown that the proposed FDTD scheme is more accurate at higher frequencies owing its different formulation, which provides second-order accuracy in both time and space. Numerical simulations of a homogeneous muscle sphere illuminated by an EM pulse were carried out. The field distributions inside the sphere were in good agreement with those obtained from Mie theory, both in the time-domain response and in the field distribution at a frequency of 500 MHz. The correctness of the algorithm for calculating energy absorbed into biological media was confirmed. In addition, physical insights into specific energy absorption, which is conventionally used as a metric, and specific energy loss were provided. Finally, simulations of illumination with an EM pulse were carried out on the detailed human head model of TARO and HANAKO, and the transient specific energy loss was also calculated. It was found that the EM pulse can penetrate deep tissues and SA peaks often occur in the CSF tissue due to its high conductivity. As

a result, the obtained SA values can be used in compliance with international standards. Further studies are to investigate the temperature elevation due to EM pulse exposure, a compliance study on various human subjects, and the extension of the proposed method to various EM applications such as ground penetrating radar and medical imaging.

Acknowledgments

This study was financially supported by the JSPS Grant-in-Aid for Scientific Research (JP18K18376), Japan, and part of the numerical calculations were carried out on the TSUBAME3.0 supercomputer at Tokyo Institute of Technology (Project number: hp190078).

References

[1] T. Zhou, M. Yang, K. Jiang, H. Wong, and D. Yang, "MMW radar-based technologies in autonomous driving: A review," Sensors, vol.20, no.24, p.7283, 2020.
[2] K. Fukunaga, Y. Ogawa, S.I. Hayashi, and I. Hosako, "Terahertz spectroscopy for art conservation," IEICE Electron. Express, vol.4, no.8, pp.258–263, 2007.
[3] T. Fukuchi, N. Fuse, M. Mizuno, and K. Fukunaga, "Nondestructive testing using terahertz waves," IEEJ Trans. PE, vol.135, no.11, pp.647–650, 2015.
[4] M. Kebe, R. Gadhafi, B. Mohammad, M. Sanduleanu, H. Saleh, and M. Al-Qutayri, "Human vital signs detection methods and potential using radars: A review," Sensors, vol.20, no.5, p.1454, 2020.
[5] J. Shi, D. Anzai, and J. Wang, "Channel modeling and performance analysis of diversity reception for implant UWB wireless link," IEICE Trans. Commun., vol.E95-B, no.10, pp.3197–3205, Oct. 2012.
[6] C. Garcia-Pardo, C. Andreu, A. Fornes-Leal, S. Castelló-Palacios, S. Perez-Simbor, M. Barbi A. Valles-Lluch, and N. Cardona, "Ultrawideband technology for medical in-body sensor networks: An overview of the human body as a propagation medium, phantoms, and approaches for propagation analysis," IEEE Antennas Propag. Mag., vol.60, no.3, pp.19–33, 2018.
[7] M. Converse, E.J. Bond, B.D. Veen, and C. Hagness, "A computational study of ultra-wideband versus narrowband microwave hyperthermia for breast cancer treatment," IEEE Trans. Microw. Theory Techn., vol.54, no.5, pp.2169–2180, 2006.
[8] W. Shao, A. Edalati, T.R. McCollough, and W.J. McCollough, "A time-domain measurement system for UWB microwave imaging," IEEE Trans. Microw. Theory Techn., vol.66, no.3, pp.2265–2275, 2018.
[9] J.C. Lin, "On microwave-induced hearing sensation," IEEE Trans. Microw. Theory Techn., vol.25, no.8, pp.605–613, 1977.
[10] C.K. Chou, A.W. Guy, and R. Galambos, "Auditory perception of radio-frequency electromagnetic fields," The Journal of the Acoustical Society of America, vol.71, no.6, pp.1321–1334, 1982.
[11] H.P. Schwan and K.R. Foster, "RF-field interactions with biological systems: Electrical properties and biophysical mechanisms," Proc. IEEE, vol.68, no.1, pp.104–113, 1980.
[12] K.R. Foster, "Thermal and nonthermal mechanisms of interaction of radio-frequency energy with biological systems," IEEE Trans. Plasma Sci., vol.28, no.1, pp.15–23, 2000.
[13] J.C. Weaver, K.C. Smith, A.T. Esser, R.S. Son, and T.R. Gowrishankar, "A brief overview of electroporation pulse strength-duration space: A region where additional intracellular effects are expected," Bioelectrochemistry, vol.87, pp.236–243, 2012.
[14] J.C. Lin, "The microwave auditory effect," IEEE J. Electromagn. RF Microw. Med. Biol., vol.6, no.1, pp.16–28, 2022, DOI: 10.1109/JERM.2021.3062826.
[15] I.G. Abidor, V.B. Arakelyan, L.V. Chernomordik, Y.A. Chizmadzhev, V.F. Pastushenko, and M.P. Tarasevich, "Electric breakdown of bilayer lipid membranes: I. The main experimental facts and their qualitative discussion," J. Electroanalytical Chemistry and Interfacial Electrochemistry, vol.104, pp.37–52, 1979.
[16] H.P. Schwan and K. Li, "Hazards due to total body irradiation by radar," Proc. IRE, vol.44, no.11, pp.1572–1581, 1956.
[17] A.R. Shapiro, R.F. Lutomirski, and H.T. Yura, "Induced fields and heating within a cranial structure irradiated by an electromagnetic plane wave," IEEE Trans. Microw. Theory Techn., vol.19, no.2, pp.187–196, 1971.
[18] P.W. Barber, "Electromagnetic power deposition in prolate spheroid models of man and animals at resonance," IEEE Trans. Biomed. Eng., vol.BME-24, no.6, pp.513–521, 1977.
[19] J.C. Lin, W. Chuan-Lin, and C.K. Lam, "Transmission of electromagnetic pulse into the head," Proc. IEEE, vol.63, no.12, pp.1726–1727, 1975.
[20] S. Gabriel, R.W. Lau, and C. Gabriel, "The dielectric properties of biological tissues: III. Parametric models for the dielectric spectrum of tissues," Phys. Med. Biol., vol.41, no.11, pp.2271–2293, 1996.
[21] T. Hosono, "Numerical inversion of Laplace transform and some applications to wave optics," Radio Sci., vol.16, no.6, pp.1015–1019, 1981.
[22] K. Moten, C.H. Durney, and T.G. Stockham, Jr., "Electromagnetic pulsed-wave radiation in spherical models of dispersive biological substances," Bioelectromagnetics, vol.12, no.6, pp.319–333, 1991.
[23] S. Masuda, S. Kishimoto, and S. Ohnuki, "Reference solutions for time domain electromagnetic solvers," IEEE Access, vol.8, pp.44318–44324, 2020.
[24] K.S. Yee, "Numerical solution of initial boundary value problems involving Maxwell's equations in isotropic media," IEEE Trans. Antennas Propag., vol.14, no.3, pp.302–307, 1966.
[25] A. Taflove and S.C. Hagness, Computational Electrodynamics: the Finite-Difference Time-Domain Method, Artech House, 2005.
[26] J. Chakarothai, K. Wake, and S. Watanabe, "Scalable GPU-parallelized FDTD method for analysis of large-scale electromagnetic dosimetry problems," ACES J., vol.31, no.6, pp.661–668, 2016.
[27] J.Y. Chen and O.P. Gandhi, "Currents induced in an anatomically based model of a human for exposure to vertically polarized electromagnetic pulses," IEEE Trans. Microw. Theory Techn., vol.39, no.1, pp.31–39, 1991.
[28] T. Kashiwa, Y. Ohtomo, and I. Fukai, "A finite-difference time-domain formulation for transient propagation in dispersive media associated with Cole–Cole's circular ARC law," Microw. Opt. Techn. Lett., vol.3, no.12, pp.416–419, 1990.
[29] R. Luebbers, F.P. Hunsberger, K.S. Kunz, R.B. Standler, and M. Schneider, "A frequency-dependent finite-difference time-domain formulation for dispersive materials," IEEE Trans. Electromagn. Compat., vol.32, no.3, pp.222–227, 1990.
[30] C.M. Furse, J.-Y. Chen, and O.P. Gandhi, "The use of the frequency-dependent finite-difference time-domain method for induced current and SAR calculations for a heterogeneous model of the human body," IEEE Trans. Electromagn. Compat., vol.36, no.2, pp.128–133, 1994.
[31] J. Chakarothai, S. Watanabe, and K. Wake, "Numerical dosimetry of electromagnetic pulse exposures using FDTD method," IEEE Trans. Antennas Propag., vol.66, no.10, pp.5397–5408, 2018.
[32] H.H. Abdullah, H.A. Elsadek, H.E. ElDeeb, and N. Bagherzadeh, "Fractional derivatives based scheme for FDTD modeling of nth-order cole–cole dispersive media," IEEE Antennas Wireless Propag Lett., vol.11, pp.281–284, 2012.
[33] D. Caratelli, L. Mescia, P. Bia, and O.V. Stukach, "Fractional-calculus-based FDTD algorithm for ultrawideband electromagnetic characterization of arbitrary dispersive dielectric materials," IEEE Trans. Antennas Propag., vol.64, no.8, pp.3533–3544, 2016.

[34] J. Chakarothai, "Novel FDTD scheme for analysis of frequency-dependent medium using fast inverse laplace transform and Prony's method," IEEE Trans. Antennas Propag., vol.67, no.9, pp.6076–6089, 2019.
[35] J. Chakarothai, K. Wake, S. Watanabe, Q. Chen, and K. Sawaya, "Frequency-dependent FDTD method for ultra-wideband electromagnetic analyses," IEICE Trans. Electron. (Japanese edition), vol.J102-C, no.5, pp.102–113, May 2019.
[36] S. Kishimoto, S. Ohnuki, Y. Ashizawa, K. Nakagawa, and W.C. Chew, "Time domain analysis of nanoscale electromagnetic problems by a boundary integral equation method with fast inverse laplace transform," J. Electromagnet. Waves Appl., vol.26, no.8-9, pp.997–1006, 2012.
[37] J. Chakarothai and K. Fujii, "Retrieval of Debye parameters from Cole–Cole model for broadband FDTD analyses," 2020 International Symposium on Antennas and Propagation (ISAP), pp.1–3, 2020.
[38] O.P. Gandhi and C.M. Furse, "Currents induced in the human body for exposure to ultrawideband electromagnetic pulses," IEEE Trans. Electromagn. Compat., vol.39, no.2, pp.174–180, 1997.
[39] V.D. Santis, M. Feliziani, and F. Maradei, "Safety assessment of UWB radio systems for body area network by the FD^{2}TD method," IEEE Trans. Magn., vol.46, no.8, pp.3245–3248, 2010.
[40] K. Huang and Y. Liao, "Transient power loss density of electromagnetic pulse in debye media," IEEE Trans. Microw. Theory Techn., vol.63, no.1, pp.135–140, 2015.
[41] P.D. Smith and K.E. Oughstun, "Electromagnetic energy dissipation and propagation of an ultrawideband plane wave pulse in a causally dispersive dielectric," Radio Sci., vol.33, no.6, pp.1489–1504, 1998.
[42] P.M.T. Ikonen and S.A. Tretyakov, "Determination of generalized permeability function and field energy density in artificial magnetics using the equivalent-circuit method," IEEE Trans. Microw. Theory Techn., vol.55, no.1, pp.92–99, 2007.
[43] V. Raicu, "Dielectric dispersion of biological matter: Model combining Debye-type and "universal" responses," Phys. Rev. E, vol.60, no.4, pp.4677–4680, 1999.
[44] J.A. Roden and S.D. Gedney, "Convolution PML (CPML): An efficient FDTD implementation of the CFS–PML for arbitrary media," Microw. Opt. Technol. Lett., vol.27, no.5, pp.334–339, 2000.
[45] J.A. Stratton, Electromagnetic Theory, John Wiley & Sons, New Jersey, 2007.
[46] J.C. Lin, Electromagnetic Fields in Biological Systems, Taylor & Francis, 2012.
[47] T. Nagaoka, S. Watanabe, K. Sakurai, E. Kunieda, S. Watanabe, M. Taki, and Y. Yamanaka, "Development of realistic high-resolution whole-body voxel models of Japanese adult males and females of average height and weight, and application of models to radio-frequency electromagnetic-field dosimetry," Phys. Med. Biol., vol.49, no.1, pp.1–15, 2004.
[48] ICNIRP, "Guidelines for limiting exposure to time-varying electric, magnetic, and electromagnetic fields (up to 300 GHz). International commission on non-ionizing radiation protection," Health Phys., vol.74, no.4, pp.494–522, 1998.
[49] IEEE-C95.1, "IEEE standard for safety levels with respect to human exposure to radio frequency electromagnetic fields, 3 kHz to 300 GHz," IEEE Std C95.1-2005 (Revision of IEEE Std C95.1-1991), pp.1–238, 2006.

Jerdvisanop Chakarothai received his B.E. degree in electrical and electronic engineering from Akita University, Akita, Japan, in 2003, and his M.E. and D.E. degrees in electrical and communication engineering from Tohoku University, Sendai, Japan, in 2005 and 2010, respectively. He is now a senior researcher at the National Institute of Information and Communications Technology, Tokyo. His research areas include computational EM, biomedical communications, and electromagnetic compatibility (EMC). Dr. Chakarothai is a member of the Institute of Electronics, Information and Communication Engineers (IEICE), the Institute of Electrical Engineers, Japan (IEEJ), and the Applied Computational Electromagnetic Society (ACES). He is an expert member of IEC CISPR SC/A. He received the 2014 Young Scientist Award from the International Scientific Radio Union and the Best Presentation Award from IEEJ and IEICE in 2015 and 2018, respectively. He also received the Ulrich L. Rohde Innovative Conference Paper Award on Antenna Measurements and Application in 2018, the Invited Paper Award from the Electronics Society of the IEICE in 2020, and the Best Paper Award in International Symposium on Antennas and Propagations (ISAP) in 2021.

Katsumi Fujii received his B.Eng., M.Eng., and Ph.D. degrees in electronic engineering from the University of Electro-Communications, Tokyo, Japan, in 1996, 1998, and 2001, respectively. From 2001 to 2006, he was a research associate with the Research Institute of Electrical Communications, Tohoku University, Sendai, Japan. Since 2006, he has been with the National Institute of Information and Communications Technology, Tokyo, where he is currently a group leader of the Standard Calibration Group in the Electromagnetic Compatibility Laboratory. His current research interests include calibration methods for measurement instruments and antennas for electromagnetic interference measurements and radio equipment. Dr. Fujii is a member of the Institute of Electronics, Information and Communication Engineers.

Yukihisa Suzuki received his B.E., M.E., and D.E. degrees in nuclear engineering from Osaka University, Osaka, Japan, in 1993, 1995, and 2001, respectively. He is currently a professor with the Department of Electrical and Electronic Engineering, Tokyo Metropolitan University, Tokyo, Japan. His research interests include bio-electromagnetics, high-performance computing in many core systems, radiation interaction physics in the space environment, and plasma physics for nuclear fusion. Dr. Suzuki is a member of the Institute of Electronics, Information and Communication Engineers (IEICE) of Japan, the Institute of Electrical Engineers (IEE) of Japan, the Information Processing Society of Japan (IPSJ), the Physical Society of Japan, and the Japan Society of Plasma Science and Nuclear Fusion Research.

Jun Shibayama received his B.E., M.E., and Dr.E. degrees from Hosei University, Tokyo, Japan, in 1993, 1995, and 2001, respectively. In 1995, he joined Opto-Technology Laboratory, Furukawa Electric Co., Ltd., Ichihara, Chiba, Japan. He became an assistant of Hosei University in 1999, where he is currently a professor. His research interests include the numerical analysis of electromagnetic problems. He received the IEEE Ulrich L. Rohde Innovative Conference Paper Award on Computational Techniques in Electromagnetics in 2017, and the Best Paper Award during the International Symposium on Microwave and Optical Technology in 2017. He also received the IEICE Electronics Society Award in 2018 for his contributions to pioneering research on high-performance numerical analysis of the LOD-FDTD method. Dr. Shibayama is a member of OSA, IEEE, and ACES.

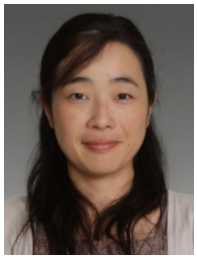

Kanako Wake received her B.E., M.E., and D.E. degrees in electrical engineering from Tokyo Metropolitan University, Tokyo, Japan, in 1995, 1997, and 2000, respectively. She is currently with the National Institute of Information and Communications Technology, Tokyo, Japan, where she is involved in research on biomedical electromagnetic compatibility. Dr. Wake is a member of the Institute of Electronics, Information and Communication Engineers, the Institute of Electrical Engineers of Japan, and the Bioelectromagnetics Society. She was the recipient of the 1999 International Scientific Radio Union Young Scientist Award.